Electronic Supplementary Material (ESI) for Nanoscale.
This journal is © The Royal Society of Chemistry 2019

Electronic Supporting Information for:

Heat Generation by Branched Au/Pd Nanocrystals: Influence of Morphology and Composition

Marta Quintanilla,[a,b] Christian Kuttner,[a] Joshua D. Smith,[c] Andreas Seifert,[d,e] Sara E. Skrabalak*[c] and Luis M. Liz-Marzán*[a,e]

[a] CIC biomaGUNE, Paseo Miramón 182, 20014 Donostia-San Sebastián, Spain.

[b] Materials Physics Department, Facultad de Ciencias, Universidad Autónoma de Madrid. Avda. Francisco Tomás y Valiente 7, 28049 Madrid, Spain.

[c] Department of Chemistry, Indiana University, Bloomington, Indiana, 47405, USA.

[d] CIC nanoGUNE, Tolosa Hiribidea 76, 20018 Donostia-San Sebastián, Spain.

[e] Ikerbasque, Basque Foundation of Science, 48013 Bilbao, Spain.

* Corresponding authors: sskrabal@indiana.edu (S.E.S.), llizmarzan@cicbiomagune.es (L.M.L.-M.)

Table of contents

Section ESI.1: Synthetic details and preliminary experiments

a) Synthetic details and characterization

Table S1. Conditions for the synthesis of Au/Pd octopods with different compositional and structural features. Volumes of 100 mM gold precursor, 10 mM palladium precursor, and octahedral Au seeds used in the overgrowth step and the surfactant used in the synthesis to tune tip sharpness.

Sample	*Volume (μL)*			*Surfactant*
	$HAuCl_4$	**H_2PdCl_4**	**Seeds**	
A	100	100	750	CTAB
B	50	100	1000	CTAC/NaBr
C	100	100	750	CTAC/NaBr
D	100	100	900	CTAC/NaBr
E	50	100	950	CTAB

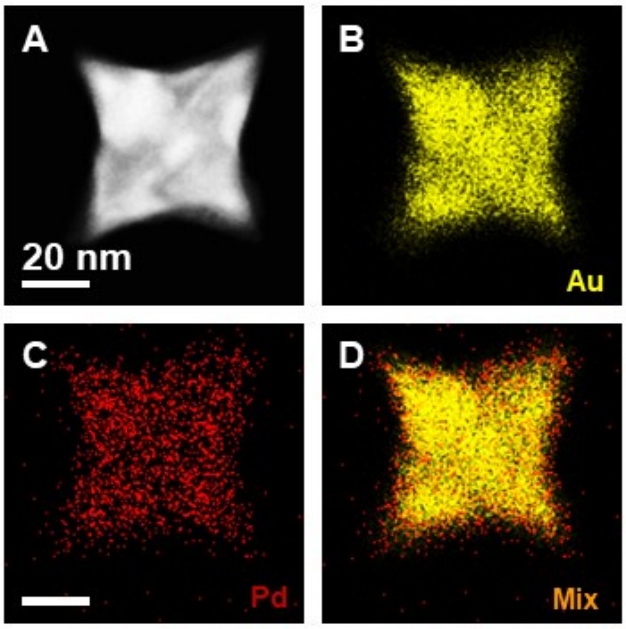

Figure S1. STEM-EDX analysis: (A) STEM image of an individual octopod (Sample B) and (B-D) corresponding elemental map obtained by STEM-EDX analysis. (B) Au only (yellow), (C) Pd only (red), and (D) overlay of Au and Pd signals.

b) Schematic geometrical representations

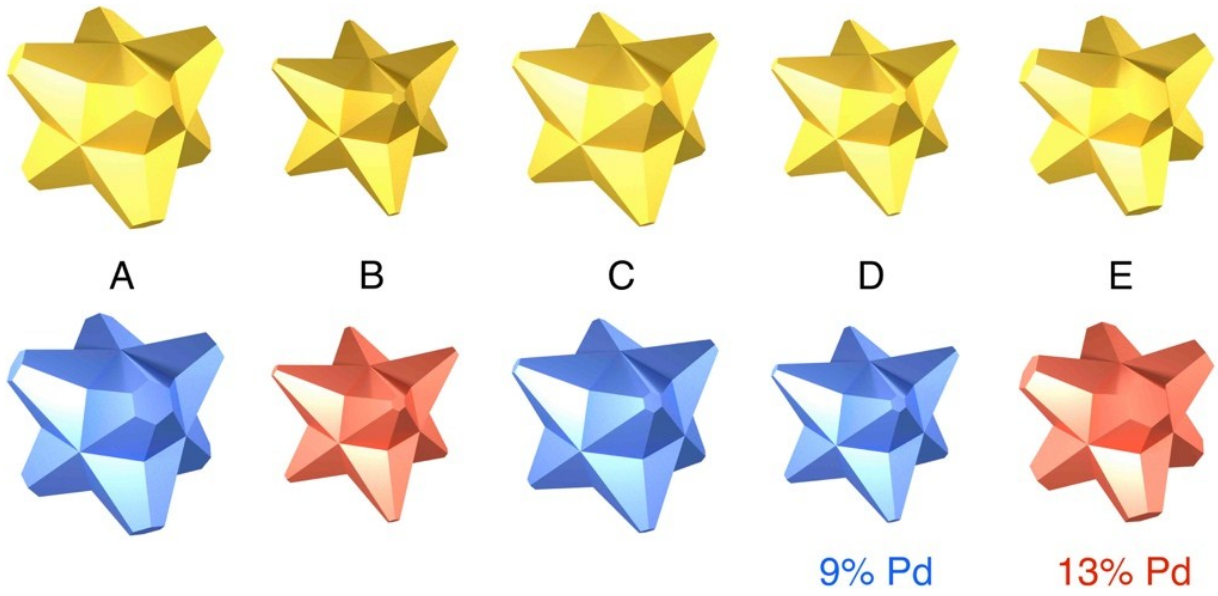

Figure S2. Schematic representation of the samples: The five samples studied in the main text are illustrated here, labelled from A to E. Their main features have been considered in this depiction: size, tip-sharpness, and palladium content (given by a colour code: red for 13 Pd% and blue for 9 Pd%).

c) Thermal stability

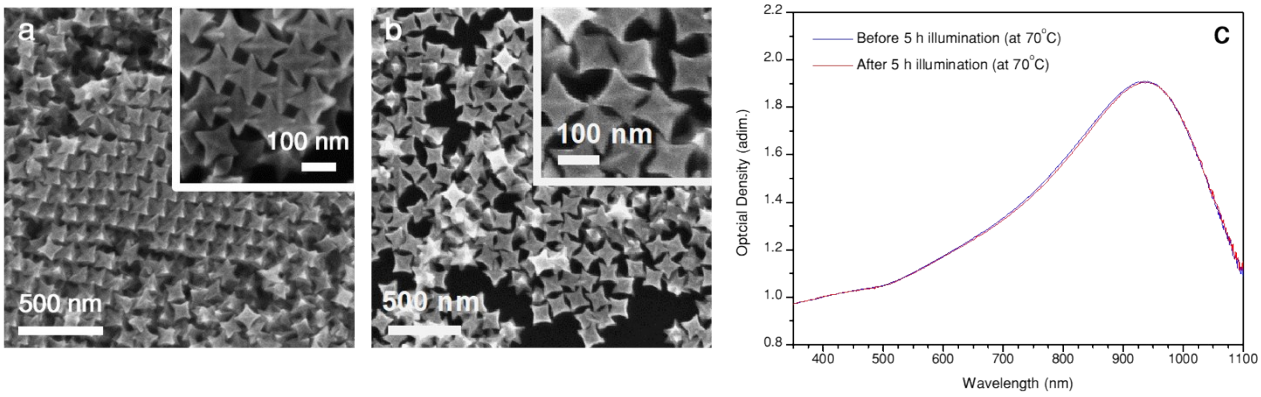

Figure S3. Thermal stability: SEM micrographs of sample B (a) before and (b) after 5 h of photothermal heating, reaching 70 °C. (c) Corresponding absorbance spectra: no changes in the optical properties could be detected (normalized at 400 nm).

Section ESI.2: Quantification of absorption and scattering losses

The spectral losses of octopod dispersions were quantified by diffuse reflectance UV/vis/NIR spectroscopy using a $BaSO_4$-coated integrating sphere (UPB-150-ART, Gigahertz-Optik, 150 mm diameter), equipped with a white-light halogen source (HL-2000-FHSA, Ocean Optics), a light trap (UPB-150-ART-Z04), and a spectrometer (MAYA Pro, Ocean Optics) as detector. For the measurements, a quartz glass cuvette with four clear sides was positioned at the centre of the integrating sphere (see **Fig. S4**) and a fixed set of measurements was performed as described by Höller *et al.*:[S1] sample measured without light trap (scattered and transmitted light); sample measured with light trap (scattered light); and water measured without light trap (as background). From this data, the absorption and scattering losses were evaluated.

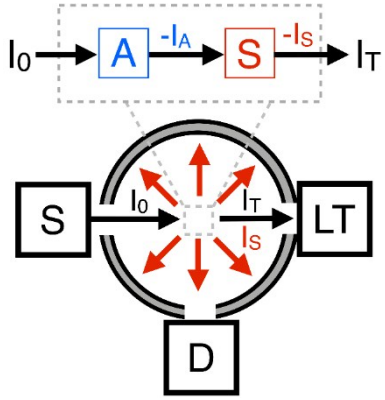

Figure S4. Schematic depiction of the diffuse reflectance setup: The light of intensity I_0 from a white light source (S) enters the integrating sphere and hits the sample positioned in the centre (dashed grey). An optional light trap (LT) is attached at the port opposite to the entry port. The opening perpendicular to the transmission axis directs the light to the detector (D). When interacting with the sample volume, absorbing (A) and scattering (S) processes may result in losses. If the light trap is present, the transmitted light (I_T) can exit the sphere and will not reach the detector.

Section ESI.3: Heating efficiency

Roper *et al.,*[S2] based on thermal equilibrium equations, developed an expression for the heating efficiency, η:

$$\eta = \frac{Q_{NP} - Q_s}{P(1 - 10^{-OD})} \tag{S1}$$

where P is the laser power, OD is the optical density measured at the laser wavelength, so the denominator in Eq. S1 is the extinguished power. Q_{NP} is the heat power released by the nanoparticles and Q_s the heat power released by the solvent. Heat power, Q_i, is defined as:

$$Q_i = \frac{mC_p}{\tau}\Delta T \tag{S2}$$

with m the mass of the suspension, C_p its heat capacity, ΔT the thermal increment when equilibrium is reached, and τ the cooling rate. In our experiment, C_p can be assumed as the heat capacity of water, as we are working with low concentrations. On that regard, it should be noted that if the concentration of particles is too low and heating too mild, the results may lose accuracy due to fluctuations of the room temperature or limitations of the thermal camera. If the concentration is too high, the results can be altered by multi-scattering interactions and by strongly inhomogeneous temperature in the sample (as light can be strongly absorbed and not reach the end of the cuvette). We have kept the optical density of the samples at the laser wavelength between 0.3 and 1.

At the illumination wavelength of our experiments, 808 nm, water is very weakly absorbing and thus Q_s can be presumed to be negligibly small. However, we quantified Q_s by performing experiments on pure water to validate that it is around 0.1% of Q_{NP}. When the laser is turned on and the sample starts to heat up until reaching the thermal equilibrium, the temperature follows an exponential rate over time. Same when the sample is cooling down, as it was shown in **Figure 3b**. The cooling rate, τ, is then the time constant of the cooling curve (in principle, one could use the heating part as well, though being the laser on, thermal gradients may interfere), and it can be calculated by measuring the evolution of the sample´s temperature over time. As an example, **Figure S5** shows the cooling curves and their fits to exponential decays of the different solutions (1 mL) with different concentrations of the five samples. Note that for the fitting we only consider the first ≈1000 s, as after that ΔT is smaller than 1 °C and the measurement becomes too noisy (consider the logarithmic scale). The time constant is a measurement of heat dissipation toward the environment and should be constant if room temperature is stable, the experimental set-up is the same, as well as the volume of sample (as it is directly linked to the dissipation surface in contact with the surroundings). However, in **Figure S5** the average τ changes a bit between the different sets of measurements, as they were recorded on different days. The other parameters in **Eq. S1** and **S2**, *i.e.*, P, m, and ΔT are straight forward to measure, and don´t need any further discussion. Consequently, we obtain one different measurement of η per concentration, that after averaging give us the final value with the error being the standard deviation.

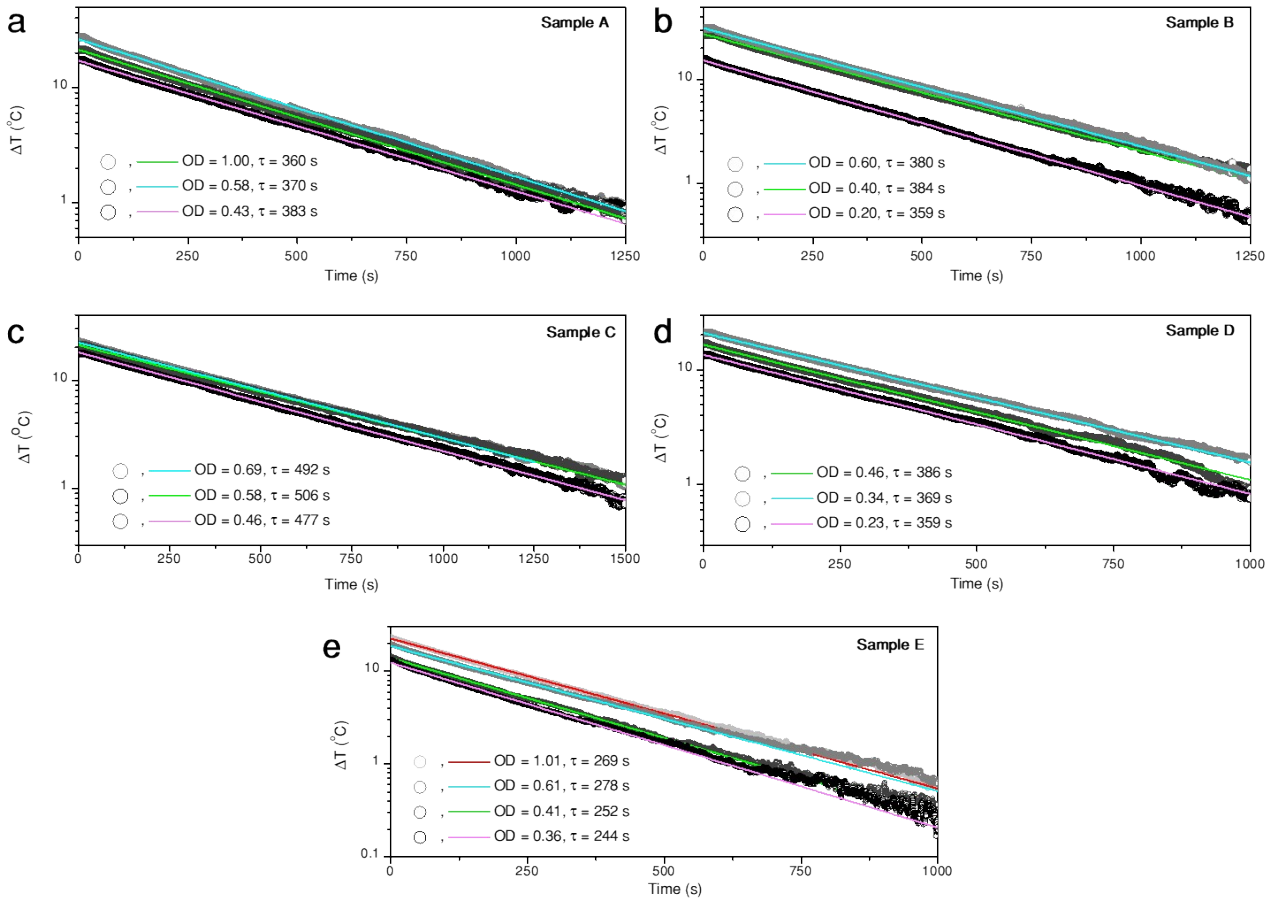

Figure S5. **Cooling down trends:** Evolution of temperature over time just after the laser was turned off (t = 0 s) measured for the five different samples in solutions with different concentrations. The dots are the experimental data and the lines are fitted to exponential decays (note the logarithmic scale). The optical density at the laser wavelengths and the time constant of each fit are given in the legends.

Section ESI.4: Octopods volume

The mathematical expression to calculate the volume, V, of octopods with identical geometry than those discussed in this manuscript was developed by deSantis et al. and is given by:[S3]

$$V = \sqrt{3}\left(\left(\frac{\sqrt{6}}{4}XY - \frac{\sqrt{2}}{2}YQ\right)(Q - Y) + \frac{\sqrt{6}}{4}XQ^2 - \frac{\sqrt{2}}{2}Q^3\right) + 2\sqrt{2}Q^3 \quad \text{(S3)}$$

Where *X*, *Y,* and *Q* are the tip-to-tip length, tip width, and tip base, respectively. Since these dimensions have been all experimentally determined and have an asociated error, we can also assign an error to *V* through errors propagation method. From the dimensions of the nanoparticles as given in **Table 1** of the main paper the volume of the nanoparticles can be determined. The obtained values are given also in **Table 1**.

Section ESI.5: Effective-medium approximation of Au/Pd alloys

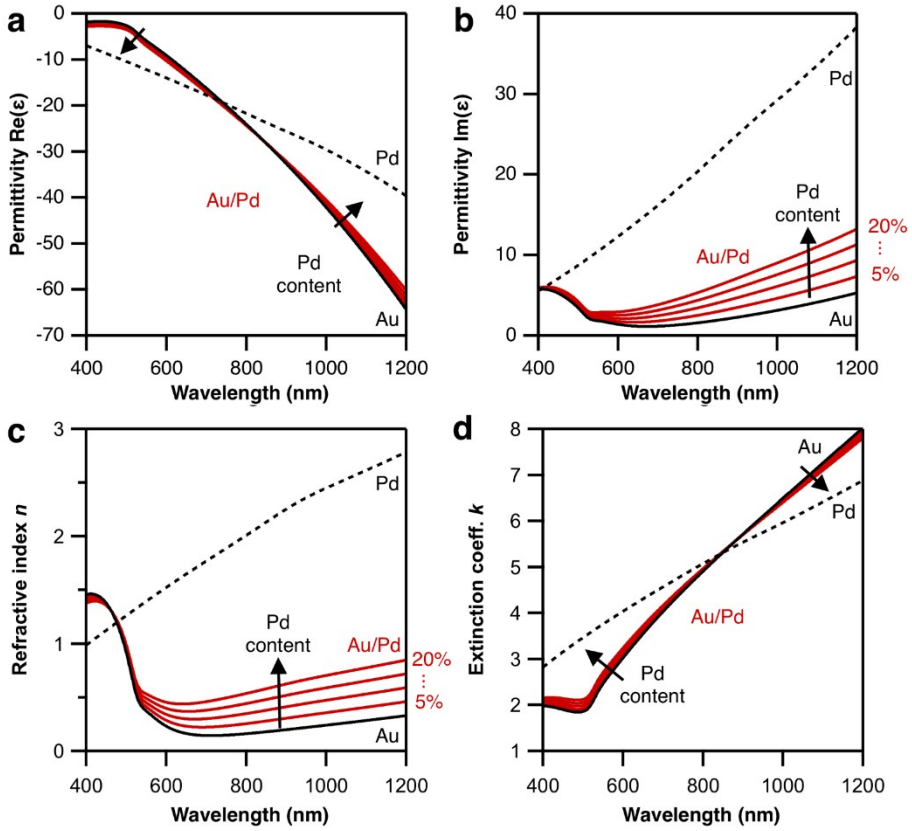

Figure S6. Maxwell-Garnett effective-medium approximation of Au/Pd alloys: (a) Real and (b) imaginary part of the permittivity and (c) refractive index and (b) extinction coefficient of gold (black line), palladium (dashed line), and Au/Pd alloys (red) with Pd contents of 5%, 10%, 15%, and 20%.

The Maxwell-Garnett equation was used to approximate the effective dielectric constant, ε_{eff}, of a mixed medium consisting of a matrix medium of Au (ε_{Au}) hosting inclusions of Pd (ε_{Pd}) with a volume fraction of δ_{Pd}:

$$\left(\frac{\varepsilon_{\mathrm{eff}}-\varepsilon_{\mathrm{Au}}}{\varepsilon_{\mathrm{eff}}+2\cdot\varepsilon_{\mathrm{Au}}}\right)=\delta_{\mathrm{Pd}}\cdot\left(\frac{\varepsilon_{\mathrm{Pd}}-\varepsilon_{\mathrm{Au}}}{\varepsilon_{\mathrm{Pd}}+2\cdot\varepsilon_{\mathrm{Au}}}\right) \tag{S4}$$

The effective dielectric constant is given by

$$\varepsilon_{\mathrm{eff}}=\varepsilon_{\mathrm{Au}}\cdot\frac{2\cdot\delta_{\mathrm{Pd}}\cdot(\varepsilon_{\mathrm{Pd}}-\varepsilon_{\mathrm{Au}})+\varepsilon_{\mathrm{Pd}}+2\cdot\varepsilon_{\mathrm{Au}}}{2\cdot\varepsilon_{\mathrm{Au}}+\varepsilon_{\mathrm{Pd}}-\delta_{\mathrm{Pd}}\cdot(\varepsilon_{\mathrm{Pd}}-\varepsilon_{\mathrm{m}})} \tag{S5}$$

Figure S6ab shows the calculated real and imaginary parts of the calculated permittivity for several compositions (δ_{Pd}), starting from pure gold (black solid line) until reaching pure palladium (black dashed line). The complex refractive index, *ñ*, can be written as a function of the dielectric constant as

$$\tilde{n}=\sqrt{\varepsilon}=\sqrt{\mathrm{Re}(\varepsilon)+i\cdot\mathrm{Im}(\varepsilon)} \tag{S6}$$

Since the real part of the complex refractive index is the refractive index, *n*, and the extinction coefficient, *k*, is the imaginary part, it can be deduced from **Eq. S6** that the real and imaginary parts of the dielectric constant can be expressed as $\mathrm{Re}(\varepsilon) = n^2 - k^2$, $\mathrm{Im}(\varepsilon) = 2nk$. Then, $n^2 = 0.5\,[\mathrm{Re}(\varepsilon) + (\mathrm{Re}(\varepsilon)^2 + \mathrm{Im}(\varepsilon)^2)^{0.5}]$, and $k^2 = 0.5\,[-\mathrm{Re}(\varepsilon) + (\mathrm{Re}(\varepsilon)^2 + \mathrm{Im}(\varepsilon)^2)^{0.5}]$. **Figure S6cd** show the refractive indices, *n*, and the extinction coefficients, *k,* calculated for several compositions of Au/Pd alloys (red).

Section ESI.6: Electromagnetic simulations

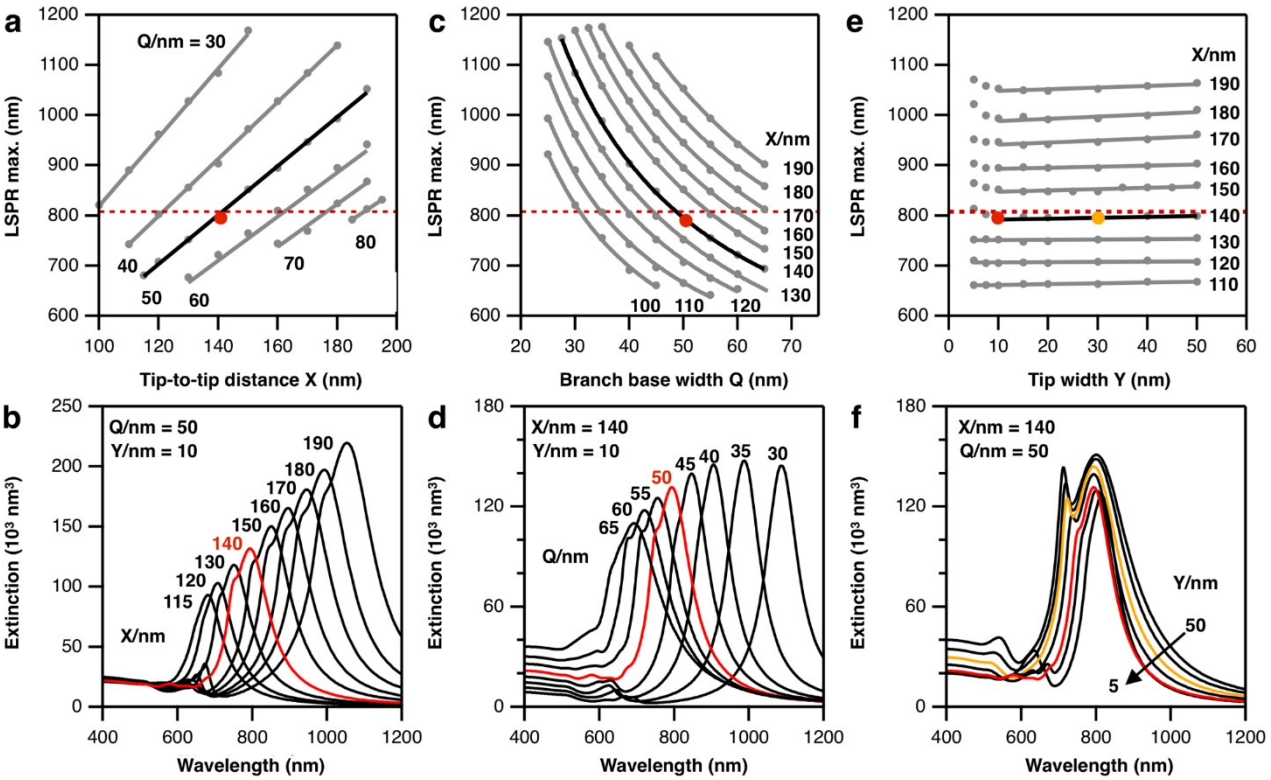

Figure S7. Influence of octopod structure and composition on optical properties: Pronounced spectral shifting of the lowest-energy plasmon mode for changes in (a,b) face diagonal size, X, and (c,d) branch width, Q, as simulated by FDTD. (e) For Y>7.5 nm, the dipolar mode is very robust against changes in tip width, as indicated by minor spectral changes in (f). The red dashed line in (a-c) indicated the laser wavelength of 808 nm.

To evaluate the influence of the individual structural parameters on the spectral position of the LSPR band maximum, we performed FDTD simulations to screen the parameter ranges of *X*/nm = [100 - 195], *Q*/nm= [25 - 65], and *Y*/nm = [5 - 50]. **Figure S7** present different plots of the obtained data to highlight the sensitivity of the LSPR for changes of a structural feature. For example, a linear-like shift toward the red can be deduced for increasing tip-to-tip distance (**Fig. S7a**)**.** Here, the width of the branch base was varied between 30 and 80 nm, while keeping the tip width of 10 nm constant (sharp tips). Surprisingly, the respective sensitivity values, given by the ratio of $\Delta\lambda/\Delta X$, are quite similar, whereas octopods with slender branches (*e.g.*, smaller *Q/Y* ratios) are more sensitive. **Fig. S7b** shows the spectral evolution of the LSPR shift for octopods with a branch base width of 50 nm (black line in **Fig. 7a**). The structure with the best match to the excitation wavelength of 808 nm is highlighted in red colour. Alternatively, the influence of the branch base width can be seen in **Fig. S7c**, keeping the tip width at 10 nm. For increasing the base width, Q, that is the transition from a tapered hexagonal prism to one with parallel sides, the LSPR shifts non-linearly toward the blue. This is exemplified for in **Fig. S7d** for a tip-to-tip distance of 140 nm. The best-match structure with *Q* = 50 nm is indicated in red colour. Finally, we regard the influence of the tip width, for a constant branch base width of 50 nm (**Fig. S7e**). Apparently, the thickness has a minor impact on the LSPR position as indicated by rather weak red shifts, as long as the tip width is above 7.5 nm (grey lines). **Figure S7f** presents the spectra changes for octopods of *X* = 140 nm and *Q* = 50 nm. The LSPR maximum remains close to 800 nm independent of the tip width. For example, sharp tips of *Y* = 10 nm (red) versus dull tips of *Y* = 30 nm (orange). Depending of the tip width, secondary higher-energy modes arise, however, of lower intensity and blue-shifting with increasing Y. Consequently,

it can be expected that these secondary modes average-out already for particle ensembles with small morphological dispersity.

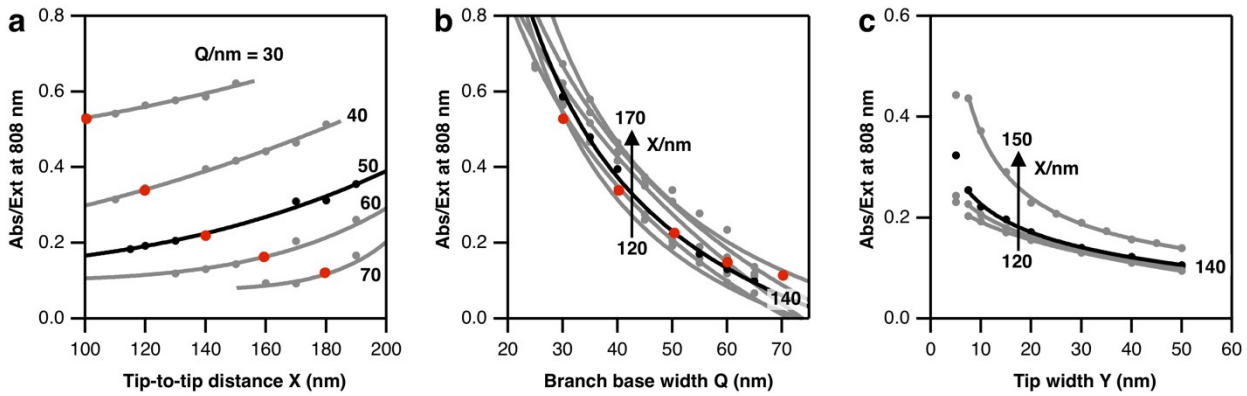

Figure S8. Influence of octopod structure on the balance of spectral contributions at 808 nm: The ratio of the absorption (Abs) to extinction (Ext) cross-sections becomes more absorbing, i.e. more beneficial for heat generation, for increasing (a) face diagonal tip-to-tip distances, decreasing (b) branch base widths, and decreasing (c) tip widths; as simulated by FDTD (note the different scales in the y-axis). Red dots highlight the parameters where extinction maximum is expected at 808 nm. They are not added to (c), as they are mostly coincident with the curve linked to *X* = 140 nm.

To further support the experimental hypothesis presented in the main paper, we investigated the influence of the structural parameters on the ratio of absorption (Abs) and extinction (Ext) by FDTD simulations. **Figure S8a** shows that the Abs/Ext ratio at 808 nm increases for larger tip-to-tip distances. Initially, this seems to contradict the general expectation that larger particles exhibit more pronounced scattering contribution. However, this is not the case. As explained in the main text, to understand Abs/Ext ratio, the position of the LSPR band must be considered with respect to the excitation wavelength. Particularly, excitation at the high-energy (shorter wavelengths) side of the LSPR maximum favours absorption over scattering; and the opposite effect occurs on the low-energy side, favouring scattering. For the sake of clarity, in the figure, the *X* and *Q* combinations that results in an extinction maximum at 808 nm are coloured in red. Then, for instance, for *Q*=50 nm (black line in **Fig. S8a**), octopods with *X* <140 nm are excited in the low-energy side, and thus favouring scattering, and octopods with *X* >140 nm are excited in the high-energy side, and thus favouring absorption. The simulations predict that larger octopods are better suited for heating at 808 nm, indicated by a more beneficial Abs/Ext ratio, as their extinction maximum will be further in the near-infrared. However, if we restrict our analysis to octopods with the extinction maximum at 808 nm (red dots), smaller particles seem better for heating, as it was deduced following **Figure 4** of the main paper.

At the same time, the width of the branch base has a significant impact on the Abs/Ext ratio (**Fig. S8b**). Following these results, octopods with slender branches (smaller Q/Y ratios) can be expected to show higher heating efficiencies. Again, the effects of LSPR-excitation mismatching discussed above (the extent of the mismatch can be deduced from the red dots, indicating a maximum at 808 nm), apply and promote light absorption when octopods are illuminated to the high-energy side of the extinction band. Finally, **Fig. S8c** shows that the tip width as well influences the Abs/Ext ratio, however, the impact of *Y* is weaker compared to *Q* (note the different scale on the y-axis). It should be noted that since *Y* is only weakly shifting the extinction maximum, effects of off-resonance illumination do not appear here.

ESI References

S1. R. P. M. Höller, M. Dulle, S. Thomä, M. Mayer, A. M. Steiner, S. Förster, A. Fery, C. Kuttner and M. Chanana, *ACS Nano*, 2016, **10**, 5740.

S2. D. K. Roper, W. Ahn and M. Hoepfner, *J. Phys. Chem. C*, 2007, **111**, 3636.

S3. C. J. DeSantis, A.C. Sue, A. Radmilovic, H.Liu, Y. B. Losovyj and S.E. Skrabalak, *Nano Lett.*, 2014, **14**, 4145.